Volume 6
Number 1
January 2021
Pages 1–60

Nanoscale Horizons

The home for rapid reports of exceptional significance in nanoscience and nanotechnology

rsc.li/nanoscale-horizons

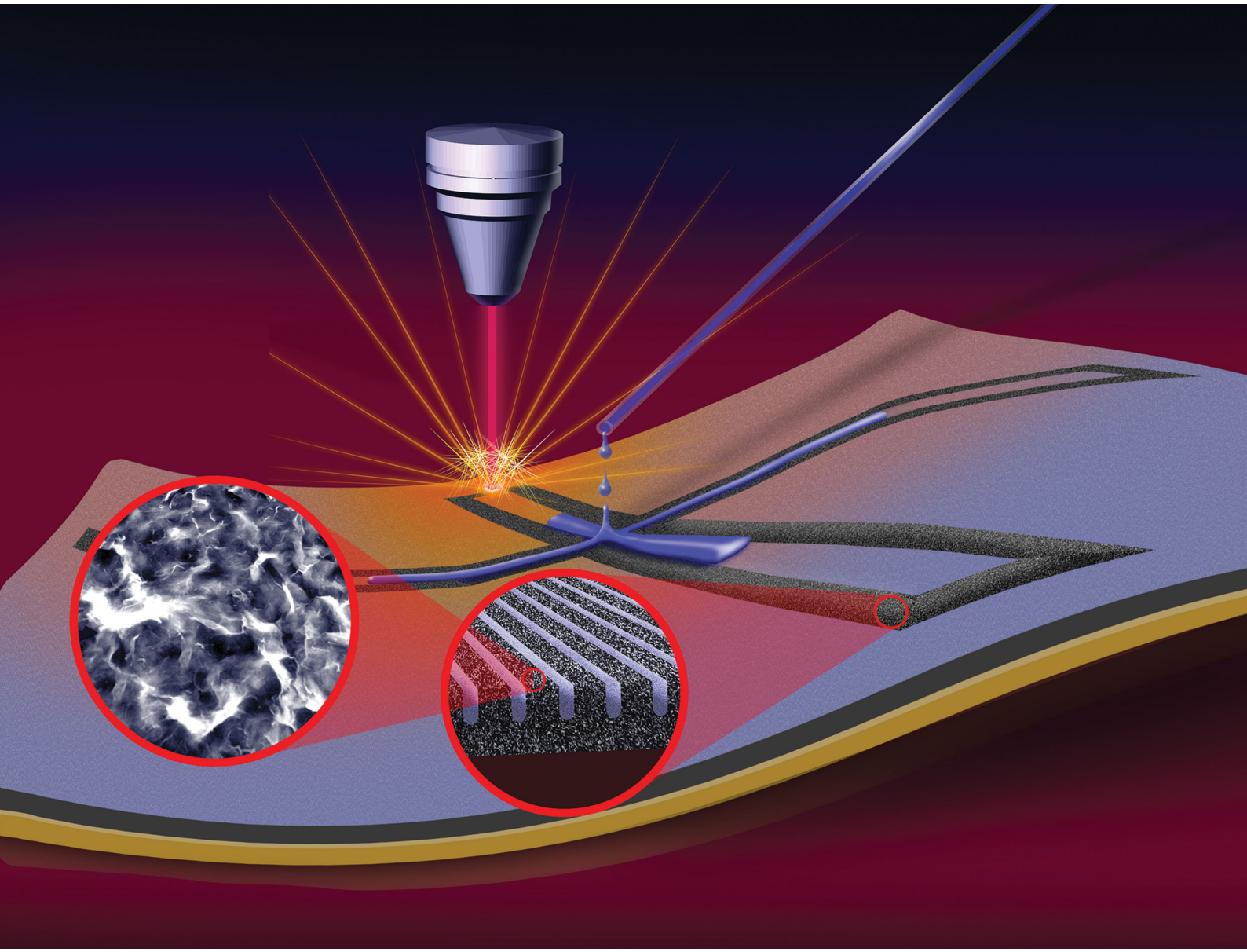

ISSN 2055-6756

ROYAL SOCIETY OF CHEMISTRY

COMMUNICATION

Michael D. Bartlett, Jonathan C. Claussen *et al.*
All-graphene-based open fluidics for pumpless, small-scale fluid transport *via* laser-controlled wettability patterning

NCNST

Nanoscale Horizons

ROYAL SOCIETY OF CHEMISTRY

COMMUNICATION

View Article Online
View Journal | View Issue

Cite this: *Nanoscale Horiz.*, 2021, 6, 24

Received 23rd June 2020,
Accepted 15th October 2020

DOI: 10.1039/d0nh00376j

rsc.li/nanoscale-horizons

All-graphene-based open fluidics for pumpless, small-scale fluid transport *via* laser-controlled wettability patterning†

Lucas S. Hall,‡[a] Dohgyu Hwang,‡§[b] Bolin Chen,‡[a] Bryan Van Belle,[a] Zachary T. Johnson,[a] John A. Hondred,[a] Carmen L. Gomes,[a] Michael D. Bartlett §*[b] and Jonathan C. Claussen *[a]

Open microfluidics have emerged as a low-cost, pumpless alternative strategy to conventional microfluidics for delivery of fluid for a wide variety of applications including rapid biochemical analysis and medical diagnosis. However, creating open microfluidics by tuning the wettability of surfaces typically requires sophisticated cleanroom processes that are unamenable to scalable manufacturing. Herein, we present a simple approach to develop open microfluidic platforms by manipulating the surface wettability of spin-coated graphene ink films on flexible polyethylene terephthalate *via* laser-controlled patterning. Wedge-shaped hydrophilic tracks surrounded by superhydrophobic walls are created within the graphene films by scribing micron-sized grooves into the graphene with a CO_2 laser. This scribing process is used to make superhydrophobic walls (water contact angle ~160°) that delineate hydrophilic tracks (created through an oxygen plasma pretreatment) on the graphene for fluid transport. These all-graphene open microfluidic tracks are capable of transporting liquid droplets with a velocity of 20 mm s^{-1} on a level surface and uphill at elevation angles of 7° as well as transporting fluid in bifurcating cross and tree branches. The all-graphene open microfluidic manufacturing technique is rapid and amenable to scalable manufacturing, and consequently offers an alternative pumpless strategy to conventional microfluidics and creates possibilities for diverse applications in fluid transport.

New concepts

We present a simple approach to develop open microfluidic platforms by manipulating the surface wettability of spin-coated graphene ink films on flexible polymers *via* laser-controlled patterning. To date, such open microfluidics have been constrained by sophisticated surface engineering techniques including photolithography with UV masks, chemical modification, among others. This is the first example of using graphene (printed or non-printed) to create a scalable manufacturing technique for open microfluidics. These open microfluidic devices permit fluid transport across the top of the graphene surface by creating narrowing, wedge-shaped hydrophilic tracks surrounded by superhydrophobic walls. These all-graphene tracks are capable of transporting liquid droplets with a velocity of 20 mm s^{-1} on a level surface and uphill at 7° elevation angles as well as transporting fluid in bifurcating cross and tree branches. Handling liquid within open microfluidics significantly minimizes the contact between the fluid and channel walls, thus eliminating or reducing the risk of channel saturation and biofouling. Additionally, these superhydrophobic sidewalls are considered antifouling. Hence, such open microfluidic platform technologies that are designed with low-cost materials could replace pumpless paper microfluidics, digital microfluidics, and conventional PMDS-based microfluidics in multiple applications including for in-field biosensors, drug discovery, emulsions formulations, and chemical flow synthesis.

Introduction

Recent advances in microfluidics, capable of performing target analyte measurements with small sample volumes, spurred the development of chemical and biological fluid analytical devices [*i.e.*, lab-on-a-chip (LOC) or miniaturized total analysis systems (mTASs)], including high throughput screening, diagnostic assays, cell biology, and drug delivery.[1] The technique is advantageous over conventional equipment that operates in off-site laboratories, owing to its rapid automated processes. Furthermore, the fluid flow in microscale channels increases the probability of bioconjugation between the target analyte and the biorecognition agent immobilized on sensors.[2] Microfluidic technologies were initially designed with materials for use in controlled laboratory settings (*e.g.*, monitoring electrophoretic phenomena, cell sorting, and micro patch clamp).[3] Rigid substrates such as silicon[4] and glass[5] were lithographically patterned and etched using cleanroom processes, interfaced with tubing/valving, and connected to various pump technologies.

[a] *Department of Mechanical Engineering, Iowa State University of Science and Technology, 528 Bissell Rd, Ames, IA 50010, USA. E-mail: jcclauss@iastate.edu*
[b] *Department of Materials Science and Engineering, Iowa State University of Science and Technology, 528 Bissell Rd, Ames, IA 50010, USA. E-mail: mbartlett@vt.edu*

† Electronic supplementary information (ESI) available. See DOI: 10.1039/d0nh00376j

‡ Equal contributors.

§ Current address: Department of Mechanical Engineering, Soft Materials and Structures Lab, Virginia Tech, Blacksburg, VA 24061, USA.

Their brittleness, intricate fabrication, and challenging channel sealing render these first-generation microfluidics unfavorable to wide-scale implementation. However, the application of polydimethylsiloxane (PDMS) to microfluidics by Whitesides revolutionized the field.[6] PDMS has been widely explored for microfluidics owing to its optical transparency, flexibility, and bonding capability with a variety of materials including glass and plastic.[7–9] One drawback is the lack of scalability to high-throughput manufacturing which presents challenges for the further development of PDMS-based microfluidics.[10] The PDMS itself has also been shown to leach uncrosslinked oligomers[11] and absorb small molecules,[12] both of which can have deleterious effects on chemical/biological sensing. Furthermore, the need for external pumps with associated tubing and connectors as well as the expense and non-degradable nature of PDMS components render this microfluidics method unsuitable for many in-field sensing/biosensing applications that require single-use, disposability.[13]

Recently, low-cost, pumpless microfluidics have been developed for in-field use even in resource limited regions.[14] For instance, paper microfluidics have emerged as an inexpensive and effective tool to provide pumpless fluid transport in numerous multiplexed detection systems including lateral flow assays.[15,16] Such paper microfluidics have been further tailored to include programmable flow rates including step changes, ramping flows, and oscillating flows[17,18] Moreover, vertical flow assay paper microfluidics have been created *via* 3D paper patterning [*i.e.*, origami microfluidic paper-analytical-devices (omPAD)] that permit applications of multistep reaction biosensors and single-cell fluidic batteries.[19] However, paper microfluidics are prone to biofouling and saturation, which can decrease the sensitivity and accuracy of diagnostic/screening assays.[20,21] Specifically, less than 50% of the total volume within the paper microfluidic reaches the detection zone, hence this low sample delivery efficiency can impede sensor detection limits and their ability to process extremely small volumes of fluid.[21] These problems of biofouling and saturation have been circumvented by creating on-surface fluid transport techniques, such as pumpless digital microfluidics.[22,23] However, digital microfluidics require external power, which can be a limiting factor in remote or resource-poor locations. To address this issue, a newer variant of digital microfluidics (*i.e.*, magnetic digital microfluidics) can be operated in a 'power-free' manner. Nevertheless, this technique requires a pre-sample preparation with magnetic particles and an application of external fields, which increase operational complexity and could interfere with biologicals being tested.[24] A promising alternative for rapid and economical microfluidic analysis is fluid transport through open surface microfluidics.

Capillary-force driven transport of liquid droplets using spatial gradients of microchannel wettability has shown promise for pumpless, non-planar liquid transport within microfluidic channels without the need for cellulose matrices.[25,26] Such microfluidics are created by developing expanding, wedge-shaped hydrophilic tracks surrounded by superhydrophobic walls. Liquid drops in open surface microfluidics are pushed forward between the non-parallel superhydrophobic walls by net Laplace pressure.[27,28] Handling liquid within these microfluidics significantly minimizes the contact between the fluid and the channel walls as compared to paper microfluidics, thus eliminating or significantly reducing the risk of channel saturation and biofouling. Additionally, these parallel superhydrophobic sidewalls are considered antifouling by hampering biomolecule adsorption and binding.[29,30] However, creating open microfluidics by tuning the wettability of surfaces typically requires sophisticated processing, which is unamenable to scalable manufacturing processes and often requires costly cleanroom processing. These fabrication processes include sophisticated surface engineering techniques such as photolithography with UV masks;[26,31,32] chemical modification (self-assembly monolayer chemistry); deep reactive ion etching;[33,34] titanium oxide nanotube fabrication in conjunction with ink patterning with contact pen drawing,[35] thermal annealing, chemical treatment, or UV illumination;[36] syringe pump controlled fountain pen printing;[37] or nanoparticle air brushing.[38,39] Moreover, a wide variety of printing techniques have been developed to create controlled surface wettability patterns on surfaces including lithographic patterning, microcontact printing and inkjet printing.[40,41] These patterning techniques demonstrate promising contact and noncontact printing processes to distinctly control wettability and even include reports of transfer printing onto single-layer graphene.[42] However, these techniques generally require lithographic patterning, photopatterning, chemical treatment with self-assembled monolayers, and/or transfer patterning, and these techniques have not been explored for use in open microfluidic applications. The work presented herein demonstrates how many of these cumbersome printing processing steps can be circumvented by controlling the surface wettability of graphene itself through direct-write laser etching or scribing.

Here, we report the first all graphene-based open microfluidics through a scalable, rapid laser patterning technique. Graphene, a type of 2-dimensional (2D) carbon material, has been explored for diverse applications including energy storage,[43] thermal management,[44] filtration,[45] and biosensing,[46,47] due to its unique and advantageous properties (*e.g.*, high electrical and thermal conductivity, surface area, as well as mechanical and thermal stability) and ease of fabrication. The graphene used in this work is also considered to be relatively inexpensive to produce due to the batch production of chemically exfoliate graphene flakes from graphite. Recently, the surface wettability of graphene has been shown to be tunable *via* selective graphene growth on patterned silicon substrates with microwave plasma chemical vapor deposition,[48] solvent dispersion,[49] and rapid-pulsed laser annealing.[50] We present a laser scribing technique that uses a CO_2 laser to scribe micron sized grooves into spin coated graphene flake films on flexible substrates [*e.g.*, polyethylene terephthalate (PET)]. The spin coated graphene is first made hydrophilic by treating the surface within an oxygen plasma environment. Next, a CO_2 laser is used to pattern micron scale grooves into the graphene to form superhydrophobic regions (water contact angle $\sim 160^\circ$) that act as

fluid flow channel boundaries for the open microfluidic tracks. These all-graphene open microfluidic tracks are capable of transporting liquid droplets with a velocity of 20 mm s^{-1} on a level surface and uphill at elevation angles of 7°. All manufacturing steps (graphene coating, plasma treatment, and laser scribing) can be performed outside of a cleanroom environment. Furthermore, channel designs can be easily created and modified with computer aided design (CAD) software, which does not require a mask nor a mold. Hence, this novel all-graphene open microfluidic manufacturing technique is economical and amenable to scalable manufacturing, which is highly applicable across diverse fluid transport applications.

Experimental

Graphene ink formulation

Graphene flake ink suitable for spin coating was formulated similar to our previously published protocols.[46,51] In summary, pristine completely reduced graphene oxide (750 mg) (ACS Materials GN1P005, 1–5 μm flake size; henceforth referred to as graphene) and ethyl cellulose (750 mg) (Sigma-Aldrich 433837) were added to a solution of terpineol (50 mL) (Sigma-Aldrich T3407) and acetone (200 mL). The colloidal solution was then probe sonicated for 4 h (Sonics Vibra-cell VCX-750 ultrasonic processor) at 70% power amplitude with a 9 s pulse and 1 s pause to break up large particles and to disperse graphene into a homogeneous mixture. The graphene ink was then placed on a hotplate (200 °C) and vigorously stirred to evaporate the acetone from the ink.

Graphene ink spin coating & oxygen plasma treatment

A portion of the graphene ink solution (3 mL) was then pipetted onto a heat-treated polyethylene terephthalate [PET (Kemafoil, Coveme TSL W)] and spin-coated at 1000 rpm for 30 seconds followed by 5 seconds at 2000 rpm. The graphene-coated PET was then placed under a heat gun for 10 minutes to remove solvents and increase adhesion between graphene and the substrate. Consecutive spin-coated and post-bake layers were repeated in an identical fashion to increase the graphene film thickness. Oxygen plasma (Harrick plasma PDC-001) was used to make the surface of the graphene ink hydrophilic. The pressure in the oxygen plasma chamber was kept at 700 mTorr during the five-minute treatment.

Superhydrophobic laser scribing

Following the oxygen plasma treatment, the samples were patterned with a CO_2 laser (Epilog Fusion Laser M2, power 75 W, wavelength λ = 10.65 μm). The laser ablation was set between 1 and 9% of the total 75 W capabilities of the laser. By using these laser settings, the patterned portions of the sample were made superhydrophobic. After studying the effects of laser settings on the surface characteristics (Fig. 3), the laser power and speed were fixed at 5% and 50% ($\sim$500 mm s^{-1}), respectively, in order to obtain the optimized performance of the superhydrophobic substrate.

Water contact angle measurements

The contact angle of water was measured using a goniometer. A droplet of water (3 μL) was dispensed onto the sample surface by an automated dispensing system (Rame-hart p/n 100-22). Images of the contact angle were generated and analyzed using ImageJ, where the value of the contact angle was estimated.

Water displacement measurements

The recorded video was analyzed by using a video analysis tool (Tracker, Open Source Physics) to measure the displacement of the water flow as a function of time. We selected the apex of the curvature of the water droplet closest to the final destination of the patterned track as the tracking point for the displacement measurement. The fluid flow rate from the syringe pump was set to 0.25 mL min^{-1}.

Scanning electron microscopy

SEM images were taken using a FEI Quanta 250 FEG Scanning Electron Microscope at a 10 kV accelerating voltage.

Data analysis

A completely randomized design was used in this study and the results were reported as mean ± standard deviation. Results were obtained by performing at least 3 independent experiments. Data analysis was performed using JMP Pro statistical software (version 15, SAS, Cary, NC).

Results and discussion

Overview of the fabrication process

The all-graphene open microfluidics were constructed following four main fabrication steps, including graphene ink formulation, graphene ink spin coating, oxygen plasma treatment, and laser scribing (see Fig. 1 & Experimental). The graphene ink was prepared by mixing completely reduced graphene oxide flakes (15 mg mL^{-1}) and ethyl cellulose within a solvent solution comprised of terpineol and acetone through probe sonication (Fig. 1a). Ethyl cellulose was chosen as a surfactant to help stabilize the graphene suspensions and has been shown to carbonize upon thermal or laser annealing, which increases the adhesion of the graphene to the substrate and reduces the electrical contact resistance within the printed film.[47,52,53] After probe sonication, graphene ink was heated at 200 °C on a hotplate to remove the acetone (Fig. 1b) and consequently to increase the viscosity of the ink to approximately 175 cP. The viscous graphene ink was coated onto a polyethylene terephthalate (PET) substrate (Fig. 1c) by using a dual-speed spin coating method and then exposed to a heat gun for 10 minutes to remove solvents and to increase adhesion between graphene and the substrate. Next, the graphene-coated substrates were exposed to an oxygen plasma treatment that rendered the surface hydrophilic by increasing the superficial oxygen species (Fig. 1d), followed by laser scribing with a CO_2 laser to create superhydrophobic patterns (Fig. 1e). This superhydrophobicity is attributed to the hierarchical micro/nanostructure of the

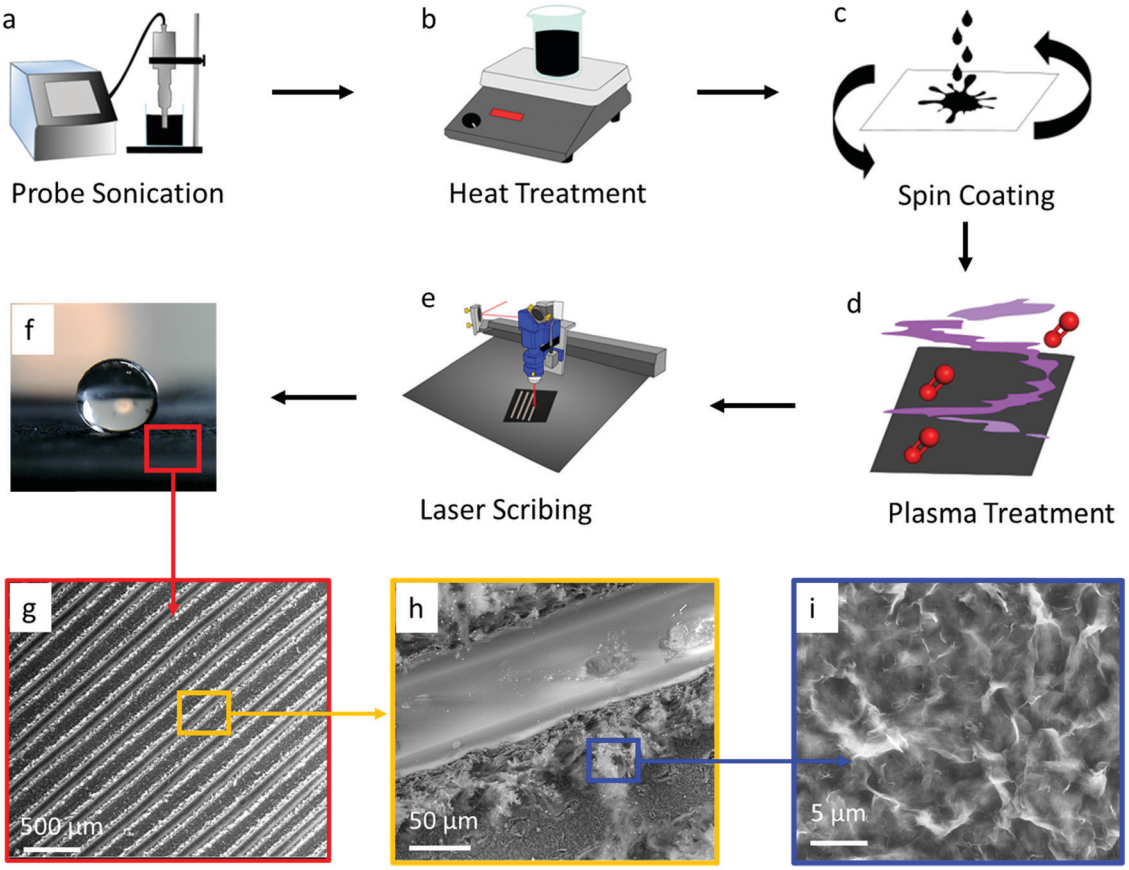

Fig. 1 Schematic diagram illustrating the fabrication protocol for the all-graphene open microfluidic. Fabrication steps include (a) graphene ink formulation and sonication, (b) thermal (200 °C) removal of acetone from the graphene ink, (c) dual-speed spin coating of the graphene ink onto a PET substrate, (d) oxygen plasma treatment of the coated graphene surface to increase the hydrophilicity of the surface, and finally (e) laser scribing to create superhydrophobic patterns on the coated graphene. (f) Image showing water droplet on superhydrophobic laser scribed graphene surface and (g–i) corresponding SEM images at incremental magnifications of the superhydrophobic graphene region.

laser patterned graphene. SEM imaging shows that the laser scribing creates lines at the tens of micron scale (Fig. 1g and h). Each of these lines is decorated with a secondary, sub-micron scale fibrillar-like roughness which is attributed to the laser ablation of the graphene surface (Fig. 1i). Together, these two scales of roughness create a hierarchical micro/nanostructure which alters the surface wettability and the surface–water adhesion. As noted by previous reports, the hydrophobicity of a surface increases as the fraction of liquid–air contact area on that surface increases.[54] Moreover, the adhesive force of a droplet on a surface is also dictated by the three-phase (solid–air–liquid) contact line (TCL) or in more discrete structures the point contact line (*i.e.*, discontinuous TCL) in addition to the fraction of liquid–air contact area. Micro/nanoporous structures such as those observed in the presented laser scribed graphene (see Fig. 1) display a high degree of discrete solid–air–liquid point contacts (*i.e.*, discontinuous TCL) which results in a low droplet adhesion force.[55] This low droplet adhesion coupled with extremely low surface wettability (*i.e.*, superhydrophobic surface) is commonly referred to as the Lotus state which is a special case of the Cassie superhydrophobic state.[56–58] The presence of a low droplet adhesion force is further corroborated by the observed low water contact angle hysteresis (*i.e.*, $\theta_a - \theta_r \approx 1^\circ$, see Fig. 3b). Subsequently, we posit that such low water surface adhesion assists with the movement of fluid through the developed graphene-based open microfluidics.

Tuning the surface wettability of the graphene surface

The first step in developing the open microfluidic patterns is to tune the surface wettability of the coated graphene from hydrophobic to superhydrophilic. After spin coating the graphene film is hydrophobic, as demonstrated by water beading up on the film surface; however, after treating the surface with oxygen plasma, the water droplet wets the graphene surface instantly, which demonstrates the superhydrophilic nature of the treated film (see Fig. S2, ESI†). The next step in creating the open microfluidic patterns is to develop the superhydrophobic boundaries through laser scribing with a CO_2 laser (see Fig. 1e & Experimental). A simple linear wedge pattern was delineated through laser scribing to create superhydrophobic boundaries that surrounded hydrophilic tracks. The surface wettability of the lased graphene was maximized by tuning the number (thickness) of spin-coated graphene layers, line spacing between lased grooves,

the power of the laser, and the laser speed settings. First, the graphene thickness and lased groove-to-groove widths were tuned, while the laser power and speed were fixed (see Experimental section). The thickness of the spin coated graphene was varied from approximately 3 μm to 30 μm by repeating the graphene spin coating process up to 10 times (Fig. 2c). Note that the thickness of the coated graphene increases by about 3 μm after each consecutive spin coating. The minimum thickness required to create a superhydrophobic surface is ~15 μm (5 spin coated layers) (Fig. 1f and 2a). Spin coated graphene thicknesses below 15 μm (5 layers) are unable to form the groove depths necessary to create superhydrophobic surfaces, while graphene thicknesses over 15 μm do not change the graphene surface wettability (Fig. 2d). Parallel experiments were also conducted to elucidate the appropriate laser scribed groove spacing. The dynamic contact angle of patterns with groove spacing between 100 μm and 400 μm was acquired. It was shown that groove-to-groove spacing between 200 and 250 μm yielded the highest increases in hydrophobicity (Fig. 2e).

All subsequent experiments were conducted accordingly with a groove spacing of approximately 250 μm, as shown in Fig. 2b. The patterned graphene was able to retain its superhydrophobic properties over time in ambient conditions as the dynamic contact angle did not significantly ($P > 0.05$) change its value over a 15 day period (Fig. 2f). Hence, this result demonstrates that such an open fluidic platform could be implemented in the field for multiple experiments over a timeframe of weeks. Additionally, with regards to the mechanical strength of the graphene coating, cyclic bending experiments were performed. The graphene films were wrapped around a 1 cm radius cylinder for multiple bending cycles. No significant changes of contact angle were observed before and after 100 bending cycles as the contact angle was 172 ± 4° before bending and 172 ± 2° after.

After the graphene ink depth (15 μm) and laser-scribed groove spacing (250 μm) were tuned for maximum resultant graphene hydrophobicity, the laser speed and power were also tuned. Speed settings from 10 to 90% of the capabilities of the 75 W laser were varied along with power settings ranging from 1 to 9% of the maximum. The advancing contact angle of the laser scribed graphene showed the maximum value of $\theta_a \approx 170°$, when laser speed was kept between 50 to 90% maximum and the power between 5 to 7% maximum (Fig. 3a). The contact angle hysteresis showed the minimum value of $\theta_a - \theta_r \approx 1°$, when the speed and power ranged from 10 to 30% and from 7 to 9%, respectively (Fig. 3b). To determine the suitable laser settings to maximize the hydrophobicity while keeping the hysteresis minimum, the ratio of the advancing contact angle to the contact angle hysteresis was plotted in Fig. 3c. The superhydrophobic nature of the graphene is maximized while hysteresis is minimized when the laser speed and power are set at approximately 50% and 5% maximum intensity, respectively. These results indicate that to achieve the superhydrophobicity, which is required for enabling the pumpless transport, the laser setting as well as the pattern geometry must be optimized. For instance, the lower power setting (1%) partially removes materials of the substrate, which results in

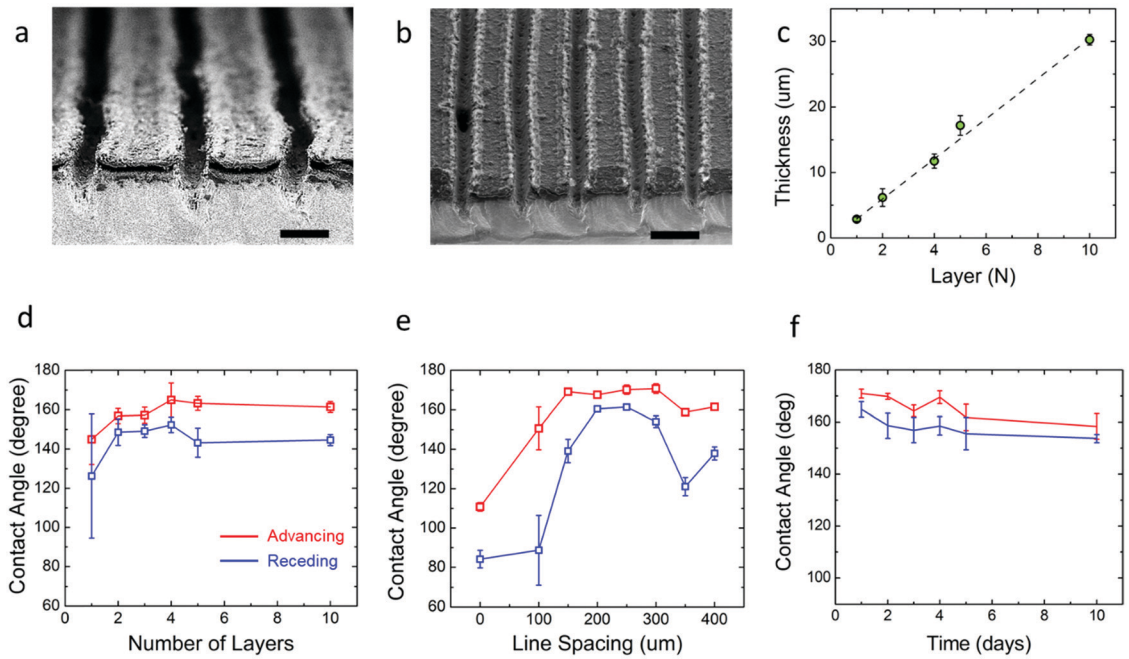

Fig. 2 SEM images of (a) cross-sectional view of the graphene surface with laser scribed grooves, scale bar 100 μm; (b) tilted view of the graphene surface to show the typical 250 μm groove width, scale bar 250 μm. (c) The graphene thickness at the corresponding number of layers that the ink was spin coated. The dynamic contact angle of the laser scribed coated graphene PET substrate. The red plots display advancing contact angle measurements while the blue plots display receding contact angle measurements (d) the dynamic contact angle *vs.* the number of layers of patterned spin-coated graphene ink with 250 μm line spacing, (e) the dynamic contact angle *vs.* the spacing of the linear pattern on 15 μm thick (5 layers) spin-coated graphene, and (f) dynamic contact angle of the lased graphene over a 15 day period.

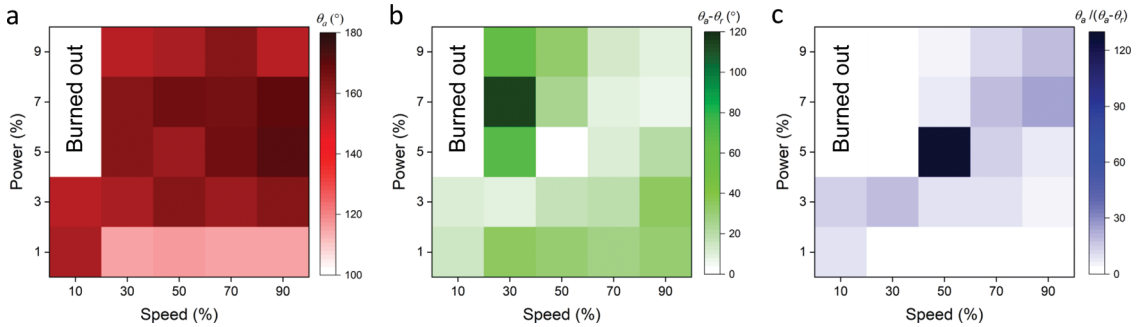

Fig. 3 Characterization of the effect of the laser speed and power settings on the surface wettability of the patterned graphene ink. (a) The advancing contact angle, (b) the contact angle hysteresis, and (c) the ratio of the advancing contact angle and the contact angle hysteresis based on the percent power *vs.* percent speed of the laser. Note that the groove depth and spacing are ~100 μm and ~250 μm, respectively. The drop volume is 3 μL.

the narrower spacing and the lower height of the patterned region. At the optimized setting, the height of the patterned region was measured to be ~100 μm (Fig. 2a). Thus, laser settings with 50% maximum speed and 5% maximum power were chosen for laser scribing in subsequent experiments.

Dynamics of fluid transport within the all-graphene open microfluidic

Next, the efficiency of transporting fluid through the all-graphene open microfluidic wedge-shaped channels with superhydrophobic boundaries and superhydrophilic tracks was analyzed (Fig. 4). A wedge angle of five degrees was used for the channel according to previous reports.[26,59] The experiments were operated by vertically dispensing a water droplet (~60 μL) containing red food coloring on the narrow end of the track and acquiring the video of droplet moving horizontally across the track (see Video S1, ESI†).

As noted in previous open microfluidics studies,[26,60,61] the liquid was transported by Laplace pressure from the narrower portion of the wedge channel towards the area of decreasing pressure along the superhydrophilic channel. To confirm that the fluid movement is indeed caused by Laplace pressure, the transport of a single-droplet of fluid was monitored on the wedge channel (Video S4, ESI†). The fluid progression halts once the drop sufficiently widens, rendering Laplace pressure too small for inducing further motion. Previous studies have explored the theory behind the transport of liquid along similar open microfluidic wedge-shaped tracks.[62] As reported by Ghosh *et al.*, the spreading of the liquid droplet occurs as the fluid volume tends to minimize its surface energy.[26] The spreading liquid bulge has a longer contact line on its leading edge as compared to its trailing edge. This leads to an unbalanced capillary force that drives the liquid volume from the narrow end to the wide end of the track.

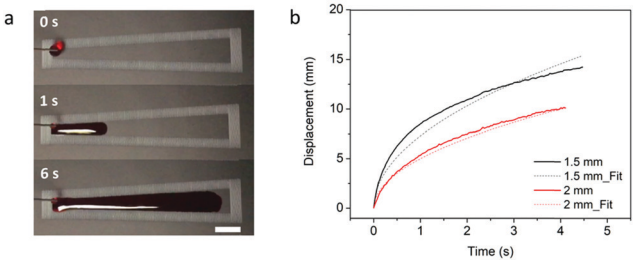

Fig. 4 Fluid transport through the all-graphene open microfluidic wedge-shaped channels. (a) Time-lapse images of water transport across a 2 mm superhydrophobic–superhydrophilic wedge-shaped wettability patterned graphene track. Images are captured at t = 0 s, 1 s, and 6 s, scale bar is 2 mm. (b) Corresponding displacement of water at different time instants for 2 mm track (red) and 1.5 mm track (black). The dots are fitting of the curve based on $x = Dt^{1/2}$ (D = 7.3 for 1.5 mm and D = 5.5 for 2 mm). Note that the groove depth, spacing, and the droplet movement distance are ~100 μm, ~250 μm, and 1.5 or 2 mm, respectively. For the geometry of the pattern, the contact angle is ~160°. The fluid flow rate from the syringe pump was set to 0.25 mL min^{-1}.

The results of the spreading behavior were studied based on the time-lapse images of fluid transport on the superhydrophobic–superhydrophilic wedge-shaped track, as shown in Fig. 4a. The relationship between the time and fluid displacement was plotted in Fig. 4b for channels with an initial channel width of 1.5 mm and 2 mm. Previous reports described the spreading behavior as an analogous to the Washburn relationship $x \sim \left(\frac{\gamma}{\mu}\right)^{1/2} t^{1/2}$, where x is the liquid-front location, t is time, γ and μ denote the fluid surface tension and viscosity, respectively.[37,60] It was found that the spreading front of the water progresses along the track as the square root of time, with dynamics similar to the wicking Washburn law inside a porous medium. The displacement-time relationship can be fitted with the equation $x = Dt^{1/2}$, where x is the displacement, and D is a coefficient. The latter is a function of the fluid surface tension and viscosity but also of the channel width. This agrees with a previous report of pumpless water spreading on hydrophilic tracks.[60] A fitting with D values of 5.5 and 7.3 for 2 mm and 1.5 mm initial channel width; respectively, are plotted in dashed lines (Fig. 4b). The fitting of 1.5 mm and 2 mm channel width (Fig. 4b) displayed good agreement with the experimental results while fitting with results garnered from a 1 mm channel did not (Fig. S1, ESI†). This lack of fit could be attributed to a narrow channel for the 1 mm case, as there is insufficient superhydrophilic channel surface area to properly transport the fluid. This can also be observed from the experimental data (the displacement is not smooth). Also, with the reduced initial

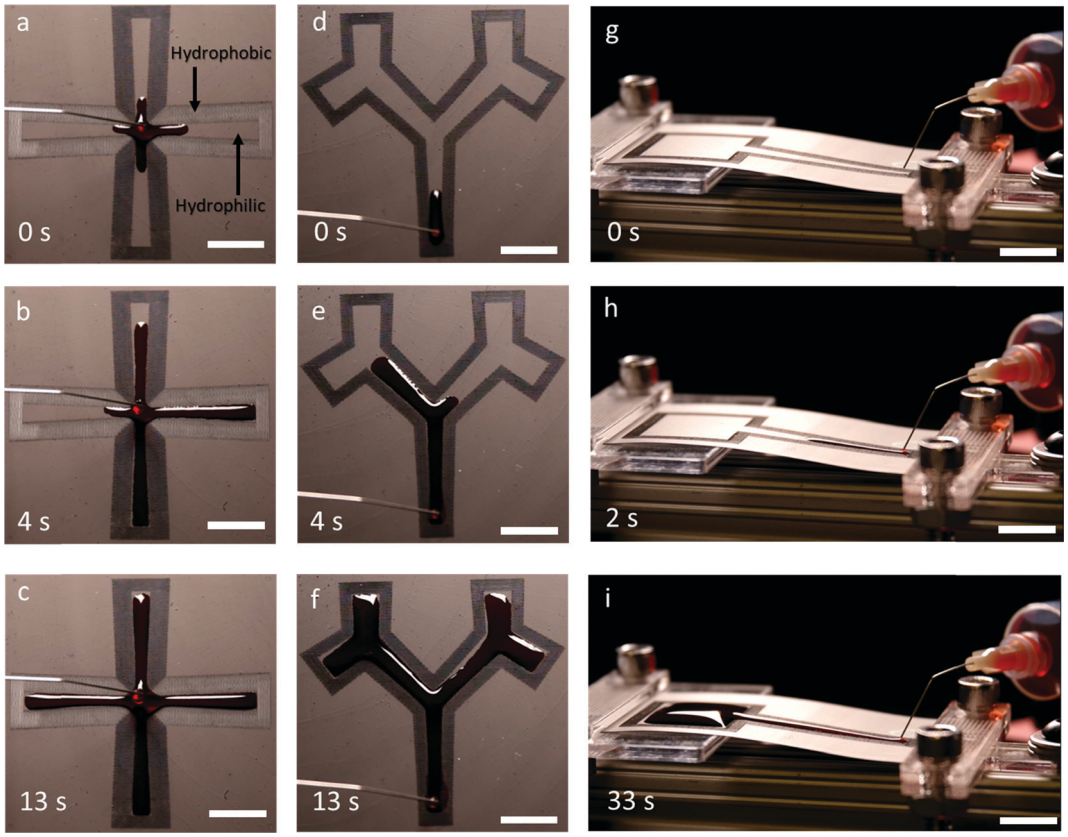

Fig. 5 Progression of fluid flow in the all-graphene microfluidics patterned in the shape of cross and tree patterns. (a) Initial, (b) continued, and (c) saturated flow in a cross pattern. (d) Initial, (e) continued, and (f) saturated flow in a tree pattern. Pumpless uphill movement (g) initial, (h) continued, and (i) saturated; all scale bars are 10 mm. Note that the groove depth and spacing are ~100 μm, ~250 μm, respectively. For the geometry of the pattern, the contact angle is ~160°. The flow rate out of the syringe for all experiments is 0.25 mL min^{-1}.

channel width from 2 mm to 1 mm, the parameter D was increased. With the controlled volume of the droplet, we believe D is proportional to the height of the spreading liquid front. Further investigation is needed to find the correlation of D and physical parameters of channels such as channel width and channel angle, which is beyond the focus of this work.

Next, in order to demonstrate the fluid transport properties at low volume flow rates, we choose two commonly used patterns (cross and tree patterns, Fig. 5a–f). The samples were tested by dispensing droplets from the tip of a controlled flow syringe onto the starting portion of the wedge. We found that the hydrophilic patterns were filled in both representative geometries (see Videos S1 and S2, ESI†). The difference in flow travel times for reaching the end of each channel in the symmetrical structures may be attributed to the misalignment of the initial droplet touch point, intrinsic bending of the PET substrate, and defects in the patterns. We also performed a water transport test where movement up an incline was attempted with varying elevation angles between 5° and 10° (Fig. 5g–i) (see Video S3, ESI†). The maximum elevation angle that enabled water transport to the top reservoir was 7°. Smaller angles that produce a lower pressure gradient were sufficient to push the water uphill at constant volume. Uphill fluid movement at this elevation angle was able to fill the reservoir at the top of the pattern. In addition, the high-volume bulge morphology observed at the reservoir showed the excellent pinning capability of the induced superhydrophobic boundary over an extended period of continuous uphill water transport. Thus, a pumpless open fluidic with the ability to pump uphill was achieved using patterning that combined wedge shape superhydrophilic tracks and superhydrophobic backgrounds on graphene surfaces.

Conclusions

A novel method of creating wettability patterning using graphene films for pumpless liquid transport on flat and inclined substrates has been demonstrated. The combination of patterning wettability for wedge shape superhydrophilic tracks and superhydrophobic backgrounds on graphene surface was able to provide a pumpless open fluidic with the ability to pump uphill. This open fluidic platform can be rapidly produced with low-cost exfoliated flakes of graphene without advanced cleanroom processing and hence is amenable to mass production. The patterned graphene retains dynamic, superhydrophobic properties over a period of 15 days, which demonstrate the stability of such a device. These all-graphene open microfluidic tracks are capable of transporting liquid droplets with a velocity of 20 mm s^{-1} on a level surface and

uphill at elevation angles of 7°. Biosensors would make use of the beneficial features of this platform, including the reduced fouling, the easily flexible patterning, the rapid fabrication, and the variability of the flow based on patterning. Such an all-graphene open microfluidic platform also has the potential for use in diverse microfluidic applications including drug discovery,[63] emulsions formulations[64] and chemical flow synthesis.[65]

Conflicts of interest

The authors declare no competing financial interest.

Acknowledgements

J. C. C. and C. L. G. gratefully acknowledges funding support for this work by the National Science Foundation under award number CBET-17069941, CBET-1756999 and ECCS-1841649 as well as by the National Institute of Food and Agriculture, U.S. Department of Agriculture, under award number 2016-67021-25038 and 2020-04109. M. D. B. gratefully acknowledges funding support through a 3M Non-Tenured Faculty Award.

References

1 E. K. Sackmann, A. L. Fulton and D. J. Beebe, *Nature*, 2014, **507**, 181–189.
2 G. Luka, A. Ahmadi, H. Najjaran, E. Alocilja, M. Derosa, K. Wolthers, A. Malki, H. Aziz, A. Althani and M. Hoorfar, *Sensors*, 2015, **15**, 30011–30031.
3 G. Velve-Casquillas, M. Le Berre, M. Piel and P. T. Tran, *Nano Today*, 2010, **5**, 28–47.
4 H. T. G. van Lintel, F. C. M. van De Pol and S. Bouwstra, *Sens. Actuators*, 1988, **15**, 153–167.
5 D. J. Harrison, A. Manz, Z. Fan, H. Luedi and H. M. Widmer, *Anal. Chem.*, 1992, **64**, 1926–1932.
6 D. C. Duffy, J. C. McDonald, O. J. A. A. Schueller and G. M. Whitesides, *Anal. Chem.*, 1998, **70**, 4974–4984.
7 M. A. Unger, H. P. Chou, T. Thorsen, A. Scherer and S. R. Quake, *Science*, 2000, **288**, 113–116.
8 S. R. Quake and A. Scherer, *From micro- to nanofabrication with soft materials*, 2000, vol. 290.
9 E. Berthier, E. W. K. K. Young and D. Beebe, *Lab Chip*, 2012, **12**, 1224.
10 H. Becker, *Lab Chip*, 2009, **9**, 2759.
11 K. J. Regehr, M. Domenech, J. T. Koepsel, K. C. Carver, S. J. Ellison-Zelski, W. L. Murphy, L. A. Schuler, E. T. Alarid and D. J. Beebe, *Lab Chip*, 2009, **9**, 2132.
12 M. W. Toepke and D. J. Beebe, *Lab Chip*, 2006, **6**, 1484.
13 P. Yager, T. Edwards, E. Fu, K. Helton, K. Nelson, M. R. Tam and B. H. Weigl, *Nature*, 2006, **442**, 412–418.
14 A. W. Martinez, S. T. Phillips, G. M. Whitesides and E. Carrilho, *Anal. Chem.*, 2010, **82**, 3–10.
15 E. Fu, T. Liang, J. Houghtaling, S. Ramachandran, S. A. Ramsey, B. Lutz and P. Yager, *Anal. Chem.*, 2011, **83**, 7941–7946.
16 E. M. Fenton, M. R. Mascarenas, G. P. López and S. S. Sibbett, *ACS Appl. Mater. Interfaces*, 2009, **1**, 124–129.
17 A. W. Martinez, S. T. Phillips, M. J. Butte and G. M. Whitesides, *Angew. Chem., Int. Ed.*, 2007, **46**, 1318–1320.
18 D. M. Cate, J. A. Adkins, J. Mettakoonpitak and C. S. Henry, *Anal. Chem.*, 2015, **87**, 19–41.
19 N. K. Thom, G. G. Lewis, M. J. DiTucci and S. T. Phillips, *RSC Adv.*, 2013, **3**, 6888.
20 Y. Zhu, X. Xu, N. D. Brault, A. J. Keefe, X. Han, Y. Deng, J. Xu, Q. Yu and S. Jiang, *Anal. Chem.*, 2014, **86**, 2871–2875.
21 X. Li, D. R. Ballerini and W. Shen, *Biomicrofluidics*, 2012, **6**, 011301.
22 M. Abdelgawad and A. R. Wheeler, *Adv. Mater.*, 2009, **21**, 920–925.
23 M. Abdelgawad and A. R. Wheeler, *Microfluid. Nanofluid.*, 2008, **4**, 349–355.
24 Y. Zhang and N.-T. Nguyen, *Lab Chip*, 2017, **17**, 994–1008.
25 Y. Temiz, R. D. Lovchik, G. V. Kaigala and E. Delamarche, *Microelectron. Eng.*, 2015, **132**, 156–175.
26 A. Ghosh, R. Ganguly, T. M. Schutzius and C. M. Megaridis, *Lab Chip*, 2014, **14**, 1538–1550.
27 Y. Nakashima, Y. Nakanishi and T. Yasuda, *Rev. Sci. Instrum.*, 2015, **86**, 015001.
28 H. S. Khoo and F.-G. Tseng, *Appl. Phys. Lett.*, 2009, **95**, 063108.
29 N. J. Shirtcliffe and P. Roach, *Methods in Molecular Biology*, Humana Press Inc., 2013, vol. 949, pp. 269–281.
30 Y. Koc, A. J. de Mello, G. McHale, M. I. Newton, P. Roach and N. J. Shirtcliffe, *Lab Chip*, 2008, **8**, 582.
31 A. Nakajima, Y. Nakagawa, T. Furuta, M. Sakai, T. Isobe and S. Matsushita, *Langmuir*, 2013, **29**, 9269–9275.
32 M. H. Alheshibri, N. G. Rogers, A. D. Sommers and K. F. Eid, *Appl. Phys. Lett.*, 2013, **102**, 174103.
33 V. Jokinen, L. Sainiemi and S. Franssila, *Adv. Mater.*, 2008, **20**, 3453–3456.
34 V. Jokinen, R. Kostiainen and T. Sikanen, *Adv. Mater.*, 2012, **24**, 6240–6243.
35 Y. Lai, F. Pan, C. Xu, H. Fuchs and L. Chi, *Adv. Mater.*, 2013, **25**, 1682–1686.
36 K. Liu, M. Cao, A. Fujishima and L. Jiang, *Chem. Rev.*, 2014, **114**, 10044–10094.
37 T. M. Schutzius, M. Elsharkawy, M. K. Tiwari and C. M. Megaridis, *Lab Chip*, 2012, **12**, 5237.
38 P. N. Manoudis and I. Karapanagiotis, *Prog. Org. Coat.*, 2014, **77**, 331–338.
39 C.-C. Hsu and P.-H. Chen, *Int. J. Heat Mass Transfer*, 2012, **55**, 3713–3719.
40 Y. Wang, M. Zhang, Y. Lai and L. Chi, *Nano Today*, 2018, **22**, 36–61.
41 D. Tian, Y. Song and L. Jiang, *Chem. Soc. Rev.*, 2013, **42**, 5184.
42 A. Cerf, T. Alava, R. A. Barton and H. G. Craighead, *Nano Lett.*, 2011, **11**, 4232–4238.
43 M. F. El-Kady, V. Strong, S. Dubin and R. B. Kaner, *Science*, 2012, **335**, 1326–1330.
44 S. Ghosh, I. Calizo, D. Teweldebrhan, E. P. Pokatilov, D. L. Nika, A. A. Balandin, W. Bao, F. Miao and C. N. Lau, *Appl. Phys. Lett.*, 2008, **92**, 151911.

45 Y. Xu, H. Bai, G. Lu, C. Li and G. Shi, *J. Am. Chem. Soc.*, 2008, **130**, 5856–5857.
46 J. A. Hondred, L. R. Stromberg, C. L. Mosher and J. C. Claussen, *ACS Nano*, 2017, **11**, 9836–9845.
47 Q. He, S. R. Das, N. T. Garland, D. Jing, J. A. Hondred, A. A. Cargill, S. Ding, C. Karunakaran and J. C. Claussen, *ACS Appl. Mater. Interfaces*, 2017, **9**, 12719–12727.
48 J. Dong, Z. Yao, T. Yang, L. Jiang and C. Shen, *Sci. Rep.*, 2013, **3**, 1733.
49 J. Rafiee, M. A. Rafiee, Z.-Z. Z. Yu and N. Koratkar, *Adv. Mater.*, 2010, **22**, 2151–2154.
50 S. R. Das, S. Srinivasan, L. R. Stromberg, Q. He, N. Garland, W. E. Straszheim, P. M. Ajayan, G. Balasubramanian and J. C. Claussen, *Nanoscale*, 2017, **9**, 19058–19065.
51 J. A. Hondred, J. C. Breger, N. J. Alves, S. A. Trammell, S. A. Walper, I. L. Medintz and J. C. Claussen, *ACS Appl. Mater. Interfaces*, 2018, **10**, 11125–11134.
52 E. B. Secor, P. L. Prabhumirashi, K. Puntambekar, M. L. Geier and M. C. Hersam, *J. Phys. Chem. Lett.*, 2013, **4**, 1347–1351.
53 S. R. Das, Q. Nian, A. A. Cargill, J. A. Hondred, S. Ding, M. Saei, G. J. Cheng and J. C. Claussen, *Nanoscale*, 2016, **8**, 15870–15879.
54 A. B. D. Cassie and S. Baxter, *Trans. Faraday Soc.*, 1944, **40**, 546.
55 Y. Lai, X. Gao, H. Zhuang, J. Huang, C. Lin and L. Jiang, *Adv. Mater.*, 2009, **21**, 3799–3803.
56 Y. T. Cheng and D. E. Rodak, *Appl. Phys. Lett.*, 2005, **86**(14), 144101.
57 J. Lin, Y. Cai, X. Wang, B. Ding, J. Yu and M. Wang, *Nanoscale*, 2011, **3**, 1258.
58 Y. Lai, J. Huang, Z. Cui, M. Ge, K.-Q. Zhang, Z. Chen and L. Chi, *Small*, 2016, **12**, 2203–2224.
59 J. M. Morrissette, P. S. Mahapatra, A. Ghosh, R. Ganguly and C. M. Megaridis, *Sci. Rep.*, 2017, **7**, 1800.
60 U. Sen, S. Chatterjee, R. Ganguly, R. Dodge, L. Yu and C. M. Megaridis, *Langmuir*, 2018, **34**, 1899–1907.
61 E. Papadopoulou, C. M. Megaridis, J. H. Walther and P. Koumoutsakos, *ACS Nano*, 2019, **13**, 5465–5472.
62 D. Quéré, *Annu. Rev. Mater. Res.*, 2008, **38**, 71–99.
63 L. Kang, B. G. Chung, R. Langer and A. Khademhosseini, *Drug Discovery Today*, 2008, **13**, 1–13.
64 K. Schroën, O. Bliznyuk, K. Muijlwijk, S. Sahin and C. C. Berton-Carabin, *Curr. Opin. Food Sci.*, 2015, **3**, 33–40.
65 E. A. Mansur, M. Ye, Y. Wang and Y. Dai, *Chin. J. Chem. Eng.*, 2008, **16**, 503–516.

